frontiers

Time-domain Analysis of Chalcogenide Threshold Switching: from ns to ps scale

R. Brunetti [1*], **C. Jacoboni** [1], **E. Piccinini** [2] **and M. Rudan** [3]

[1] *FIM Department, University of Modena and Reggio Emilia, Modena, Italy*
[2] *Applied Materials Italia s.r.l.*
[3] *DEI Department and ARCES Research Center, University of Bologna, Bologna, Italy*

Correspondence*:
Rossella Brunetti
rossella.brunetti@unimore.it

ABSTRACT

A space- and time-dependent theoretical model based on a trap-assisted, charge-transport framework for the amorphous phase of a chalcogenide material is used here to interpret available experimental results for the electric current of nanoscale devices in the ns–ps time domain. A numerical solution of the constitutive equations of the model for a time-dependent bias has been carried out for GST-225 devices. The “intrinsic” rise time of the device current after the application of a suitable external bias is controlled by the microscopic relaxation of the mobile-carrier population to the steady-state value. Furthermore, the analysis is extended to include the effect of the external circuit on the electrical switching. A quantitative estimate of the current delay time due to unavoidable parasitic effects is made for the optimised electrical set up configurations recently used by experimental groups.

Keywords: Chalcogenides, GST, Ovonic threshold switching, Phase change memories, Charge transport, Amorphous materials

1 INTRODUCTION

Chalcogenide-based Phase Change Memories (PCM) have been studied for many years as a possible replacement for Flash memories, and in the late 2000’s eventually hit the market as storage elements for cell phones (Servalli, 2009). Furthermore, being two-terminal devices, they were easily integrated in 3D cross-point memory arrays (Optane, 2017a,b; Choe, 2017), paving the way for storage-class memories thanks to their fast access time and moderate cost per bit.

After a suitable tailoring of the chalcogenide-alloy composition, to match the specs dictated by a specific use, embedded PCM have the potential to become key enablers of technological breakthroughs in a number of industrial applications; among these, automotive applications (Arnaud et al., 2018). In recent years, PCM devices were also profitably employed in “non von Neumann” neuromorphic computing architectures, exhibiting a better performing collocation of memory and processing (Markram et al., 2011; Le Gallo et al., 2018; Sebastian et al., 2020; Sarwat et al., 2021).

Whatever application for PCM devices is envisaged, their working principle relies on the fast and reversible structural change of a chalcogenide alloy that switches between the amorphous (*reset*) and crystalline (*set*) states, upon the application of an electric pulse (Lai, 2003; Raoux and Wuttig, 2009;

Kolobov and Tominaga, 2012; Redaelli, 2019). The bottleneck of a fast electrical switching is inherent in the crystallization process, starting from the high-resistance amorphous phase (Anbarasu et al., 2012). In many cases, a voltage pulse of suitable intensity, and width of a few ns is required to surpass, first, an Ovonic Threshold Switching (OTS) event, namely an off-to-on threshold switching in the amorphous state, precursor of the amorphous-to-crystalline phase change. A useful parameter that has been introduced to quantify the transition speed is the so-called delay time t_d, defined as the time interval between the instant at which the applied voltage exceeds the threshold value and the instant at which a steep rise in the device current begins (Wimmer and Salinga, 2014; Shukla et al., 2016). Despite efforts to decrease t_d with different strategies, so far it has been difficult to obtain values below 1 ns (Wimmer and Salinga, 2014). Thus, achieving sub ns threshold-switching times for nanoscale devices is a goal of both scientific and technological relevance (Wimmer and Salinga, 2014; Saxena et al., 2021).

The exploitation of the electrical threshold switching property of many chalcogenide-based devices, for designing phase-change memory devices with access speed comparable to the SRAM, pushed experimentalists to design extremely performing and accurate measuring setups (Shukla et al., 2017). The latter must be able to respond to very fast external electric pulses, in order to precisely record the onset of the threshold switching and the change of the current value from the low value of the amorphous off state to the high value of the amorphous on state. A major attempt to provide new experimental insights into the threshold-switching mechanism by means of a precise knowledge of the exact shape of the voltage applied to the chalcogenide cell has been carried out by Salinga and coworkers (Wimmer and Salinga, 2014). According to the Authors, in the reported experiments on GST-225 devices, due to the careful impedance matching of the contact board the applied voltage pulses reach the memory cell without any significant distortion. Measurements were performed where the applied voltage signal, aimed at producing the threshold voltage, ramps up linearly from zero to a maximum value; the leading edge of the voltage ranges from few ns to 104 ns. The value at which threshold switching appears depends upon the steepness of the ramp; in particular, short rise times of the latter lead to high switching voltages, whereas the application of slow ramps produces a decrease in the switching voltage. Thus, the pulse shape strongly influences the switching voltage, so that the concept of a unique voltage at which the resistance of the cell falls becomes questionable (Wimmer and Salinga, 2014; Shukla et al., 2016).

This concept is pushed even further in a recent paper by Saxena and coworkers (Saxena et al., 2021), where it is shown that delay times in the ps scale can be obtained in GST-225 cells by means of an appropriate design of both the experimental apparatus and the external voltage applied to the cell. In particular, the Authors measured delay times shorter than 50 ps for a voltage equal to twice the threshold voltage measured in static conditions for the same material, proving that PCM memory devices can reach SRAM-like speeds. Besides the technological implications of the above-mentioned performances, experimental measurements of Ovonic threshold switching in the time domain provide new interpretation challenges to test the existing theories about the switching mechanism; such theories have been formulated mainly by Academia over the last five decades in parallel with the technological developments. While, in the low-resistance state, the standard description of conduction in semiconductors applies, the electric properties of the high-resistance state are explained as a hot-carrier effect (Ielmini, 2008; Cappelli et al., 2013; Buscemi et al., 2014a; Brunetti et al., 2020), or a combination of electro-thermal effects (Bogoslovskij and Tsendin, 2011; Le Gallo et al., 2016). Experiments where the parasitic effects have been reduced as much as possible confirm the relevance of hot-carrier phenomena on OTS, even though the high thermal efficiency and the fast thermal dynamics in nanoscale devices suggest that the heat flow dynamics can indeed play a role (Le Gallo et al., 2016).

As for the OTS effect in the amorphous phase, structural analyses and Molecular-Dynamics simulations of amorphous chalcogenides confirm the existence of a number of trap states located around mid gap, that play a fundamental role on the onset of the electrical switch (Kolobov and Tominaga, 2012; Redaelli, 2019). At low fields (below threshold) the majority of carriers are trapped and the conduction is very low; when the field is strong enough to heat the carriers, the population of the high-energy, high-mobility states is enhanced. This, in turn, increases the energy gain of the trapped carriers at the expense of the field, further enriching the population of the trap states close to the conduction-band edge (and, possibly, also band states (Brunetti et al., 2020)): in this way a positive feedback is established which, eventually, makes the current to increase by several orders of magnitude.

In this paper we apply a space- and time-dependent theoretical model based on a trap-assisted charge transport in the amorphous phase of a chalcogenide material (Piccinini et al., 2016; Jacoboni et al., 2017), to interpret the available experimental results in the ns–ps time domain for the electric current of nanoscale devices, based on the GST-225 chalcogenide, in a variety of bias conditions. A numerical solution of the constitutive equations of the model for a time-dependent bias makes it possible to test to what extent the threshold voltage depends upon the microscopic characteristic times that regulate the field-to-carrier energy transfer; this transfer is in fact responsible for the carrier heating which, in turn, produces the threshold switching. Furthermore, the analysis is extended to include the effect of the external circuit on the electrical switching, with reference to the optimised electrical set up configurations recently used by experimental groups (Saxena et al., 2021).

Sect. 2 summarizes the main features of the theoretical approach; the set of equations which constitute the model for the OTS device, and the numerical algorithm implemented for solving them, are described in Sects. 2.1–2.3, while Sect. 2.4 illustrates how we modeled the OTS device coupling with an external circuit that represents the measuring equipment. Dynamic and static models for the OTS device have been tested in view of their possible implementation into a device simulation framework. Section 3 contains our results and their critical analysis: first, parasitic effects are neglected; the ideal cases of a voltage step (Sect. 3.1) and of voltage trapezoidal profiles, similar to those reported in (Saxena et al., 2021), are considered with the purpose of evaluating the delay time of the OTS device (Sect. 3.2); then, the more realistic condition of a voltage trapezoidal profile applied to a device in presence of parasitic effects is studied (Sect. 3.3). Finally, Sect. 4 summarises the main achievements of the analysis, and provides some comments about possible developments of the present approach.

2 THEORETICAL APPROACH

The analysis aims at interpreting the experimental current-voltage curves obtained by applying time-dependent voltages with a time scale ranging from the nanoseconds to the picoseconds. Based on a thorough study of the Ovonic threshold switching by the Authors of the present paper and others (Ielmini, 2008; Piccinini et al., 2016; Jacoboni et al., 2017), the theoretical approach assumes that, when the chalcogenide material is in the amorphous phase, carrier heating due to energy transfer from the external field dominates over thermal effects in determining the OTS. Accordingly, the heat equation for the lattice is not included in the model. Carriers, here assumed to be electrons, can occupy two trap levels with energy values $E_T = 0$ and $E_B = \Delta$, with density of states g_T and g_B, respectively. Carriers in level E_T are trapped, i.e., have zero mobility and, therefore, do not contribute to the current; carriers in level E_B mimic conduction electrons, even though they have a unique well-defined energy, and contribute to the current with a constant mobility μ. The use of a single energy level for the mobile states is in fact a simplification

of the model; however, a sensible description of the physics is anyway achieved (Piccinini et al., 2016). The introduction of a dispersion relation of the mobile states improves the quantitative description of the electric switching at and above threshold, without altering the key features of the present implementation (Brunetti et al., 2020).

The device dynamics is assumed to be one-dimensional: the cross section of the sample is supposed large enough to neglect the effects of the lateral boundaries. Thus, the physical quantities of interest along the device are functions only of the longitudinal coordinate x and of time t; they are the electric field F, the total concentration of carriers n, the concentration of mobile carriers n_B, the concentration of carriers in the trap states n_T, and the particle current density j. The above quantities are not all independent from each other; in fact,

$$j = n_B\,\mu\,F - D_B\,\frac{\partial n_B}{\partial x}\,, \qquad n = n_T + n_B\,, \tag{1}$$

where D_B is the diffusion coefficient of the mobile electrons, assumed here to be given by the equilibrium Einstein relation $D_B = \mu\,k\,T_0/q$, with q the carrier charge, T_0 the room temperature, and k the Boltzmann constant. At equilibrium, the device is assumed to be spatially uniform, with an electron density n_0 neutralized by an equal density of opposite fixed charges. Furthermore, assuming Maxwellian distributions, the densities of carriers in the traps and in the mobile states are given by

$$n_{T0} = C_0\,g_T\,\exp\left[-\frac{E_T}{k\,T_0}\right] = C_0\,g_T\,, \qquad n_{B0} = C_0\,g_B\,\exp\left[-\frac{E_B}{k\,T_0}\right] = C_0\,g_B\,\exp\left[-\frac{\Delta}{k\,T_0}\right]\,. \tag{2}$$

The normalization constant C_0 is obtained from the total electron density n_0, leading to:

$$n_{T0} = \frac{n_0}{1 + (g_B/g_T)\,\exp[-\Delta/(k\,T_0)]}\,, \qquad n_{B0} = \frac{n_0}{1 + (g_T/g_B)\,\exp[\Delta/(k\,T_0)]}\,. \tag{3}$$

In presence of an electric field $F(x,t)$, electrons gain energy; furthermore, the excitation energy to reach the upper level is reduced by the field according to the Poole model (Poole, 1916), to become

$$\Delta'(x,t) = \Delta - \gamma\,|F(x,t)|\,, \tag{4}$$

with γ a suitable constant.[1] Out of equilibrium we assume that an electron temperature $T_e(x,t)$ is defined, such that the electron populations, in analogy with (3), read

$$\tilde{n}_T(x,t) = \frac{n(x,t)}{1 + (g_B/g_T)\,\exp[-\Delta'/(k\,T_e)]}\,, \qquad \tilde{n}_B(x,t) = \frac{n(x,t)}{1 + (g_T/g_B)\,\exp[\Delta'/(k\,T_e)]}\,, \tag{5}$$

It is worth noting that a variation of the electric field $F(x,t)$ is instantaneously accompanied by a variation of the activation energy Δ', while the carriers require some time to adjust their occupations to the new situation. Thus, the above quantities $\tilde{n}_B(x,t)$ and $\tilde{n}_T(x,t)$ are to be considered "tendential" values (Jacoboni et al., 2017).

2.1 Equations

The model is based on a set of four differential equations, each encoding a basic physical principle.

[1] Elsewhere the Poole-Frenkel model, viz, $\Delta' = \Delta - \gamma'\,\sqrt{|F|}$ (Jacoboni et al., 2017) is used in the description of electron transport in chalcogenides. The Poole model adopted here is usually appropriate for large concentrations of traps (Ielmini and Zhang, 2007). The theoretical development presented in this paper can include either approach.

i. Particle continuity: only charges in the mobile states can move, so that the rate of change of electron density at a given position x reads:

$$\frac{\partial n}{\partial t} = -\frac{\partial j}{\partial x}\,, \tag{6}$$

ii. Local particle redistribution: as indicated in (6), particles that cross the device at the position x come from mobile states. The rate of change of the concentration n_B accounts for redistribution between trap and mobile states, and reads

$$\frac{\partial n_B}{\partial t} = \frac{\partial n}{\partial t} - \frac{n_B - \tilde{n}_B}{\tau_n}\,, \tag{7}$$

where τ_n is the mobile-carrier relaxation time, taken as a model parameter, and $\tilde{n}_B$ is given by (5).

iii. Energy continuity: the energy density ϵ^t at (x,t) is given by $n_B\,\Delta$ since $E_T = 0$. Its variation accounts for the power density pumped by the field, the space variation of the energy flux $j\,\Delta$, and the energy relaxed to the phonon bath which, in this case, is described by a temperature-relaxation time τ_T Buscemi et al. (2014b):

$$\frac{\partial \epsilon^t}{\partial t} = q\,j\,F - \Delta\,\frac{\partial j}{\partial x} - n\,\frac{k\,T_e - k\,T_0}{\tau_T}\,. \tag{8}$$

On the other hand, differentiating the total energy $\epsilon^t(x,t) = n_B\,\Delta$, and using (7), yields

$$\frac{\partial \epsilon^t}{\partial t} = \Delta\,\left[\frac{\partial n}{\partial t} - \frac{n_B - \tilde{n}_B}{\tau_n}\right]\,.$$

Combining this result with (8) and using (6) provides

$$q\,j\,F = n\,\frac{k\,T_e - k\,T_0}{\tau_T} + \Delta\,\frac{\tilde{n}_B - n_B}{\tau_n}\,. \tag{9}$$

This equation indicates that the power provided by the field is partially dissipated to the phonon bath, and partially devoted to distribute the electrons between trapped and mobile states. This equation allows for the evaluation of the electron temperature in terms of the other unknowns. However, T_e appears also in $\tilde{n}_B$, so that the equations must be solved numerically.

iv. Poisson equation: the local carrier density $n(x,t)$ is related to the local field $F(x,t)$ by the Poisson equation:

$$\frac{\partial F}{\partial x} = \frac{1}{\varepsilon}\,\rho = -\frac{q}{\varepsilon}\,\Big[n(x,t) - n_0\Big]\,, \tag{10}$$

where ε is the material's absolute permittivity.

It is worth observing that in steady state the second term at the right hand side of (9) vanishes due to (7); it follows that τ_n has no influence on the steady-state behavior of the OTS device (more comments on this are made in Sect. 3.1).

2.2 Constraints

The four equations (6), (7), (9) and (10) govern the process we are interested in, and are solved, e.g., for the unknowns n, F, n_B, and T_e. All other variables of interest can be calculated from the set above. A number of conditions are imposed on the unknowns:

a) The electron temperature at the injecting contact is equal to the equilibrium temperature at all times:

$$T_e(0,t) = T_0\,. \tag{11}$$

b) At the source boundary of the device, the contact injects the electrons which are necessary to maintain local electric neutrality at all times:

$$n(0,t) = n_0\,, \tag{12}$$

which implies:

$$\left.\frac{\partial n(x,t)}{\partial t}\right|_{x=0} = 0 \qquad \left.\frac{\partial F(x,t)}{\partial x}\right|_{x=0} = 0$$

(the second of the above derives from (10)). Finally,

c) an integral condition on the field is imposed by the voltage $V_P(t)$ across the device:

$$V_P(t) = -\int_0^L F(x,t)\,\mathrm{d}x\,, \tag{13}$$

where L is the device length.

The model illustrated above is of the hydrodynamic type, namely, it assumes that neither the lattice temperature nor the relaxation time τ_T vary within the operating time scale of the device. This is justified by the fact that the effects of lattice heating can be neglected below threshold and do not alter the intrisic time scale of the device above threshold (Piccinini et al., 2016).

2.3 Numerical solution

The non-linear system of equations outlined in Sects. 2.1, 2.2 is solved by iterations, starting from the equilibrium condition $n(x,0) = n_0$, $F(x,0) = 0$, $n_B(x,0) = n_0/[1 + (g_T/g_B)\,\exp[\Delta/(k\,T_0)]$, and $T_e = T_0$; the time and space derivatives are approximated by finite differences. Once the unknowns are known at time t, their updated values at $t + \delta t$ are obtained with the following procedure:

1. The update $n(x, t + \delta t)$ is derived from (6).
2. Equations (5) and (7) provide the update $n_B(x, t + \delta t)$.
3. The update $F(x, t + \delta t)$ is obtained from (10) apart from the constant $F(0, t)$, which is found by imposing condition (13). The latter, in turn, is to be considered as prescribed if the device is in a standalone situation, that is, connected to a voltage generator; if, instead, the device is connected to an external circuit, V_P must be derived from the solution of the device-circuit system.
4. The update $T_e(x, t + \delta t)$ is obtained from (9). Due to the strong non-linearity of this equation and the strict requirement of a positive solution, the combined bracketing and bisection techniques (Press et al., 1988, Sect. 9.1) proved to be more efficient and stable than other iterative methods like, e.g., the Newton-Raphson method.

2.4 Circuit model

In realistic conditions, the device under investigation is coupled with an external circuit that represents the measuring equipment. Following (Piccinini et al., 2016), the simplest circuit used in studying the response of an Ovonic device to an external bias includes the Ovonic device in series with a load resistance R_L and a waveform generator $V(t)$. From the viewpoint of the external circuit, the contacts enclosing the

chalcogenide layer can be represented by a contact resistance R_S and a parasitic capacitance C_S; wirings and probes introduce a further parallel parasitic capacitance C_C. The resulting circuit is sketched in Fig. 1, where the Ovonic device is indicated with P, and $C = C_S + C_C$.

The inclusion of the circuit into the simulation can be done at different levels of completeness. The first, more general level (Sect. 2.4.1), couples the circuit with a numerical model of the Ovonic device; with respect to that illustrated in Sects. 2.1, 2.2, here the model is simplified by assuming that the device is homogeneous, while the dynamic aspects of the Ovonic device, as described by the relaxations times, are kept. The second level, less expensive from the numerical standpoint (Sect. 2.4.2), couples the external circuit with a static model of the Ovonic device, namely, a model of the form $I_P(V_P)$.

2.4.1 Coupling the circuit with a dynamic PCM model

To express the voltage drop V_P across the Ovonic device, in the circuit model we assume a constant-field approximation, which is acceptable for devices longer than 10 nm (Piccinini et al., 2016). It follows $V_P = L\,F(t)$, whence $V = R_L\,I + L\,F + A\,R_S\,J_P$, with A the cross sectional area of the metallic plates and $J_P = q\,j$ the current density across the Ovonic device. Using (1) after neglecting the diffusive term yields a relation between the field and the mobile carrier concentration:

$$F = \frac{V - R_L\,I}{L + A\,R_S\,q\,\mu\,n_B}\,. \tag{14}$$

To complete the coupling with the external circuit, another equation is necessary; in it, the voltage drop V_P must appear, which is in turn determined from the microscopic model accounting for the relaxation times. One notes from Fig. 1 that $V - V_P = R_L\,I + R_S\,(I - C\,\dot{V}_C)$, with $V_C = V - R_L\,I$; combining these two relations yields the equation sought,

$$R_S\,R_L\,C\,\dot{I} + (R_L + R_S)\,I + V_P = R_S\,C\,\dot{V} + V\,, \tag{15}$$

where the right hand side is prescribed. Equations (14, 15) are then added to (6, 7, 9) to determine the electric performance of the OTS cell (Piccinini et al., 2016).

2.4.2 Coupling the circuit with a static PCM model

Still considering the circuit of Fig. 1, the static characteristic of the PCM is sketched as shown in Fig. 2; the approximation of considering a piecewise-linear characteristic has the advantage of affording an easy analytical approach.[2] Letting $R_1(R_2)$ be the resistance of the lower (upper) branch ($R_1 \gg R_2$), it follows that the resistance of the series made of P and the heater is $R_C^- = R_1 + R_S$ when $V_P < V_{\rm th}$ and $R_C^+ = R_2 + R_S$ when $V_P > V_{\rm th}$; balancing the currents at the upper node of P yields, for $V_P < V_{\rm th}$,

$$C\,\dot{V}_C + \frac{V_C}{R_C^-} = \frac{V - V_C}{R_L}\,, \qquad \dot{V}_C + \frac{V_C}{\tau_C^-} = \frac{V}{\tau_L}\,, \tag{16}$$

[2] In principle, the approximation of a piecewise-linear characteristic could be avoided: one may in fact invert $V_C = V_P + R_S\,I_P(V_P)$ to extract $I_P(V_C)$, then solve $C\,\dot{V}_C + I_P(V_C) = (V - V_C)/R_L$ for V_C, with $V = V(t)$ prescribed. This procedure would require a separate solution of a non-linear equation in different regions of V_C.

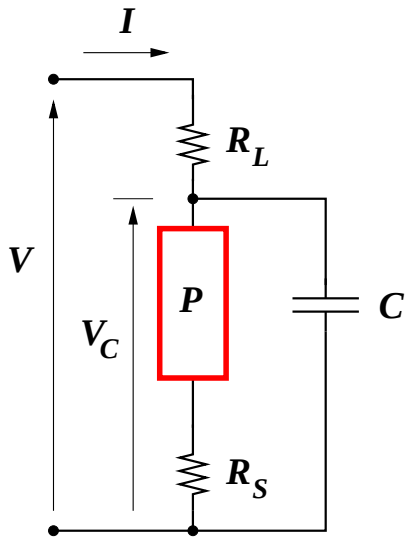

Figure 1. Circuit embedding the PCM (Piccinini et al., 2016). Parameters referred to the PCM take suffix P in the equations and figures.

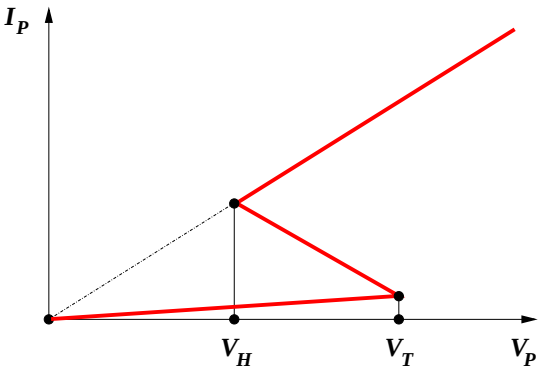

Figure 2. Schematic model of the S-shaped $I_P(V_P)$ characteristic of the PCM.

223 with $\tau_L = R_L\,C$ and $\tau_C^- = R_C^-\,\tau_L/(R_C^- + R_L)$, this yielding

$$V_C\,\exp(t/\tau_C^-) = V_C(t_0)\,\exp(t_0/\tau_C^-) + Y\,, \qquad Y = \frac{1}{\tau_L}\int_{t_0}^{t} \exp(\theta/\tau_C^-)\,V(\theta)\,\mathrm{d}\theta\,. \tag{17}$$

224 As mentioned above, here the applied voltage is a ramp, $V = \alpha\,t$, whence

$$Y = \frac{\alpha\,\tau_C^-}{\tau_L}\,(t - \tau_C^-)\,\exp\left(\frac{t}{\tau_C^-}\right) + \frac{\alpha\,\tau_C^-}{\tau_L}\,(\tau_C^- - t_0)\,\exp\left(\frac{t_0}{\tau_C^-}\right)\,. \tag{18}$$

225 In the first part of the ramp it is $t_0 = 0$, $V_P < V_{\mathrm{th}}$, $V_C(t_0) = 0$, and

$$V_C = \frac{\alpha\,(\tau_C^-)^2}{\tau_L}\,\left[\frac{t}{\tau_C^-} - 1 + \exp\left(-\frac{t}{\tau_C^-}\right)\right]\,. \tag{19}$$

The voltage across P is related to V_C by $V_C = V_P\,(1 + R_S/R_1)$, and reaches the threshold value at a time $t_{\rm th}$ such that

$$V_{\rm th} = \frac{\alpha\,(\tau_C^-)^2/\tau_L}{1 + R_S/R_1}\,\left[\frac{t_{\rm th}}{\tau_C^-} - 1 + \exp\left(-\frac{t_{\rm th}}{\tau_C^-}\right)\right]\,. \tag{20}$$

The $V_C(t)$ relation (19) is nonnegative and monotonic in the interval $0 \le t \le t_{\rm th}$. When t reaches $t_{\rm th}$, the resistance of P changes abruptly, so that $R_C^- = R_1 + R_S$ and $R_C^+ = R_2 + R_S \ll R_C^-$; due to the capacitor connected in parallel, voltage V_C is continuous at $t_{\rm th}$, so that the current $(V - V_C)/R_L$ provided by the bias is continuous as well. On the other hand, current I_P flowing through P is discontinuous at $t_{\rm th}$ (specifically, I_P increases due to the decrease in resistance); as the extra current is supplied by the capacitor, it follows that $\dot V_C^+ \neq \dot V_C^-$. If necessary, the variation in $\dot V_C$ can be evaluated from (16): writing (16) at $t_{\rm th}^-$ and $t_{\rm th}^+$, and subtracting, yields

$$C\,\dot V_C^+ = C\,\dot V_C^- - \frac{R_C^- - R_C^+}{R_C^-\,R_C^+}\,V_C < C\,\dot V_C^-\,. \tag{21}$$

In the second part of the ramp ($t > t_{\rm th}$) it is $t_0 = t_{\rm th}$, $V_P > V_{\rm th}$, and

$$V_C(t_{\rm th}) = \frac{\alpha\,(\tau_C^-)^2}{\tau_L}\,\left[\frac{t_{\rm th}}{\tau_C^-} - 1 + \exp\left(-\frac{t_{\rm th}}{\tau_C^-}\right)\right]\,. \tag{22}$$

Here the equation to be solved has the same form as (16), with R_C^- replaced with R_C^+ and τ_C^- replaced with $\tau_C^+ = R_C^+\,\tau_L/(R_C^+ + R_L)$; using again the ramp one finds

$$V_C = V_C(t_{\rm th})\,\exp\left(\frac{t_{\rm th} - t}{\tau_C^+}\right) + \frac{\alpha\,(\tau_C^+)^2}{\tau_L}\,\left[\left(\frac{t}{\tau_C^+} - 1\right) + \left(1 - \frac{t_{\rm th}}{\tau_C^+}\right)\,\exp\left(\frac{t_{\rm th} - t}{\tau_C^+}\right)\right]\,. \tag{23}$$

The quantity to be measured is the current $(V - V_C)/R_L$ provided by the bias, namely, using (19) for $0 \le t \le t_{\rm th}$,

$$I^- = \frac{\alpha}{R_L}\,t - \frac{\alpha\,(\tau_C^-)^2}{R_L\,\tau_L}\,\left[\frac{t}{\tau_C^-} - 1 + \exp\left(-\frac{t}{\tau_C^-}\right)\right]\,, \tag{24}$$

or, using (23) for $t \ge t_{\rm th}$,

$$I^+ = \frac{\alpha}{R_L}\,t - \frac{V_C(t_{\rm th})}{R_L}\,\exp\left(\frac{t_{\rm th} - t}{\tau_C^+}\right) - \frac{\alpha\,(\tau_C^+)^2}{R_L\,\tau_L}\,\left[\left(\frac{t}{\tau_C^+} - 1\right) + \left(1 - \frac{t_{\rm th}}{\tau_C^+}\right)\,\exp\left(\frac{t_{\rm th} - t}{\tau_C^+}\right)\right]\,. \tag{25}$$

The asymptotic behavior of the current, obtained from (24) and (25) is, respectively,

$$I^- = \frac{\alpha\,t}{R_L + R_1 + R_S}\,, \qquad I^+ = \frac{\alpha\,t}{R_L + R_2 + R_S}\,. \tag{26}$$

3 SIMULATION RESULTS

The voltage pulse generated by experimental equipments varies from zero to its maximum programmed value in a finite time which, at present, can be as short as few ns (Wimmer and Salinga, 2014; Saxena et al., 2021). Thus, every "real" voltage pulse contains, *de facto*, ramps with rise and fall times of finite duration; this implies the existence of a time transient of the electrical response of the device, during

which the internal electric field increases or decreases. This effect may or may not be relevant according to how the rise time compares with the time scale of the microscopic processes responsible for the carrier heating at the origin of OTS, and whether or not the maximum voltage applied to the device exceeds the threshold voltage for the Ovonic switch. The simulations discussed in this section explore different physical situations of a GST-225 chalcogenide device, starting from ideal cases where circuit parasitic elements are absent and the external pulses have negligible rise times, then moving towards conditions closer to the experimental reality. Aim of the study is to test our theoretical model, based on hot-carrier effects, against experimentally-detected electric properties of amorphous chalcogenides, on time scales around and below the nanosecond, obtained from the last experimental results appeared in the literature (Saxena et al., 2021). In absence of information about the cross-sectional area of the devices employed in the experiments, the value $5{,}000$ nm^2 has been used in all simulations to convert current densities obtained from the simulations into charge currents.

3.1 The ideal case: the voltage step

The exploration starts from the ideal case of negligible parasitic effects and negligible rise time of the applied voltage. Assuming a step-shaped voltage profile, the time dependence of the quantities relevant for transport are due only to the microscopic parameters of the model (such parameters are listed in Tab. 1). Some parameters are known from experiments, while others can be tuned on the basis of the details of the $I_P(V_P)$ characteristic for a variety of bias conditions. A preliminary study about the influence of the microscopic parameters on the transport results obtained from the present model is reported in (Jacoboni et al., 2017); there, in particular, the microscopic parameter τ_T of (8) has been proven to control the heating process of the carriers for a given internal field and, consequently, the value of the threshold voltage. In the same paper, however, a discrepancy was found between the delay time t_d predicted by the model (of the order of tens of ps) and the much longer experimental values (possibly also influenced by parasitic effects).

In a recent paper by (Saxena et al., 2021) for GST-225, the experimental steady-state OTS voltage ($V_{\rm th}$) for a device of lenght $L = 53$ nm, obtained with very long leading/trailing edges of the applied voltage, is $V_{\rm th} = 2.0 \pm 0.1$ V. This value corresponds to a threshold field $E_{\rm th} \sim 10^7$ V/m, and compares well with that obtained in (Jacoboni et al., 2017) for $\tau_T = 0.15$ ps. Consequently, this value for τ_T is also used in the present paper. The electric measurements in the time domain also reported in (Saxena et al., 2021) allow for a theoretical test on the second microscopic parameter τ_n of (7), which rules the relaxation of the mobile carrier population to the steady state value for a given applied field.

Based on the set of parameters of (Jacoboni et al., 2017), a batch of simulations is presented here for different values of τ_n in order to assess the effect of this parameter on the rise time of the current after the application of a voltage step above threshold (here the value $V = 2.4$ V has been used for the voltage step). The results are reported in Fig. 3; while no effect of the variation of τ_n has been found on the threshold value, it is seen that a delay time of about 1 ns (that is, in the same range of the experiments (Saxena et al., 2021)) is achieved with $\tau_n = 0.6$ ns, thus demonstrating that the theoretical model can be tuned in such a way as to compare well with experiments in the nanosecond scale.

Furthermore, Fig. 4 shows current I_P as a function of time for different values of the step voltage: the higher the voltage, the shorter the delay time of the current, yielding a delay shorter than a ns at the largest biases considered. This behaviour is in agreement with experimental evidence (Saxena et al., 2021).

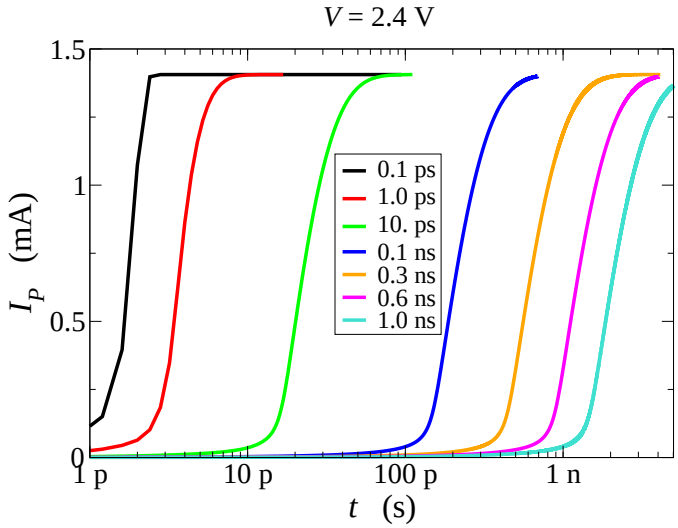

Figure 3. Current flowing across the PCM device as a function of time after the application of a 2.4 V external voltage step at $t = 0$. Different values for the microscopic parameter τ_n have been tested.

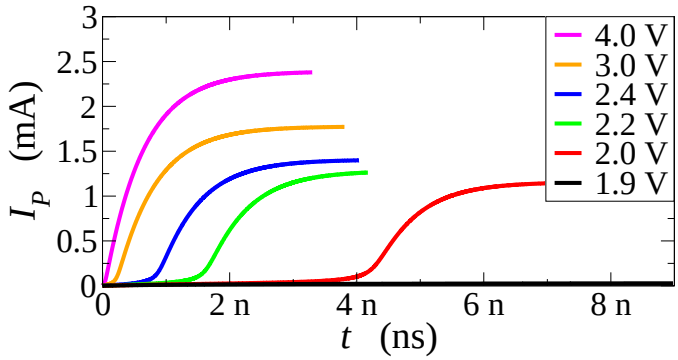

Figure 4. Current flowing across the PCM device as a function of time after the application of voltage steps of different amplitudes. The microscopic parameter τ_n has been set to 0.6 ns.

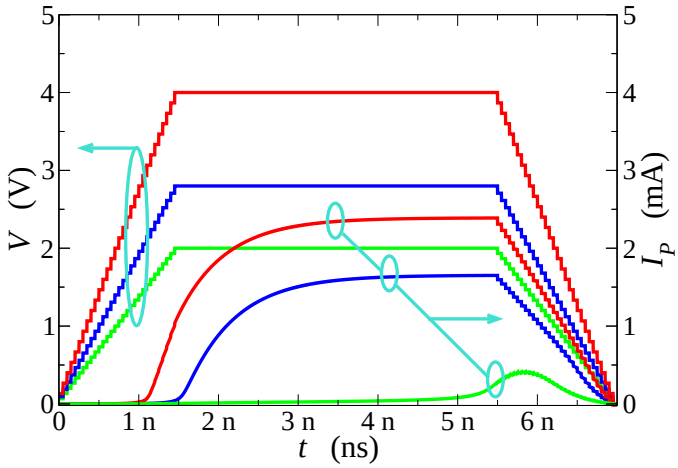

Figure 5. Current flowing across the PCM device as a function of time (right scale) after the application of voltage trapezoidal profiles of different amplitude (left scale). In all cases, rise and fall times are 1.5 ns and the duration of the plateau is 4 ns.

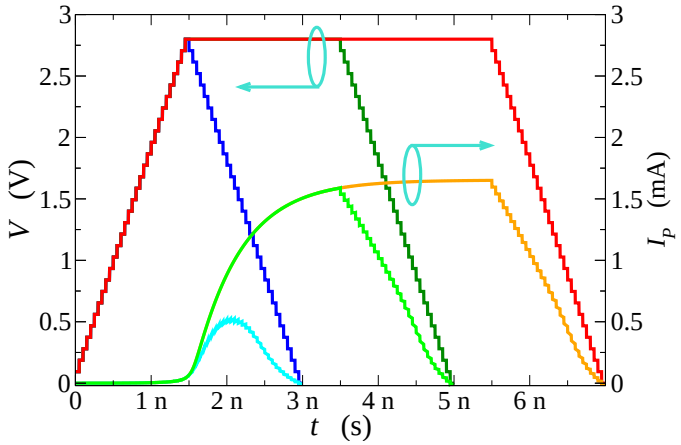

Figure 6. Current flowing across the PCM device as a function of time (right scale) after the application of voltage trapezoidal profiles of 2.8 V amplitude (left scale). Rise and fall times are 1.5 ns in all cases, whereas the plateau durations are 0, 2, and 4 ns.

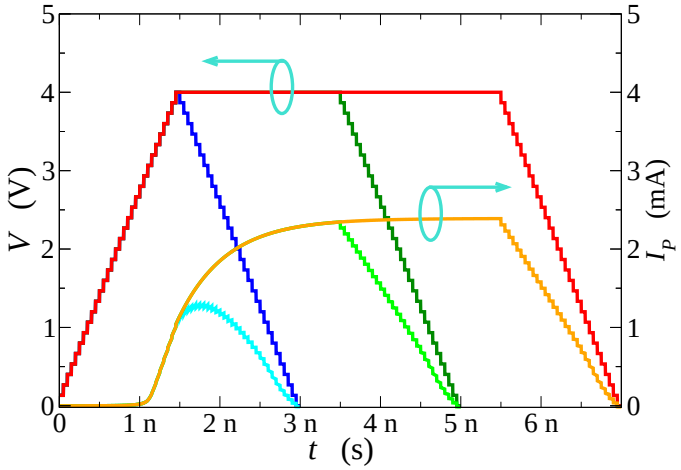

Figure 7. Current flowing across the PCM device as a function of time (right scale) after the application of voltage trapezoidal profiles of 4 V amplitude (left scale). Rise and fall times are 1.5 ns in all cases, whereas the plateau durations are 0, 2, and 4 ns.

3.2 Towards the real world: finite rise and fall times, no parasitic effects

A step towards realistic bias conditions is achieved by considering that external waveform generators provide pulses with finite rise and fall times. Top-level equipments generate voltage pulses with rise and fall times as fast as 1 ns, and with 1.5 ns Full-Width Half Maximum (FWHM) (Saxena et al., 2021). These times are comparable with the microscopic relaxation times that govern the heating process and are assumed to be responsible for the OTS effect. Thus, still in absence of parasitic effects, a comparison of the theoretical predictions with the experimental scenario on a ns time scale has been carried on with reference to the bias conditions reported in (Saxena et al., 2021).

Figure 5 reports the current flowing across the GST layer, as a function of time, due to the application of a trapezoidal profile with 1.5 ns rise and fall times, and a 4 ns duration of the plateau. Different values of the plateau have been considered, ranging from 2 V (corresponding to the OTS voltage) up to 4 V. Figures 6 and 7 report similar data for 2.8 and 4 V plateau amplitudes, respectively, with plateau durations of 0, 2, and 4 ns in each case.

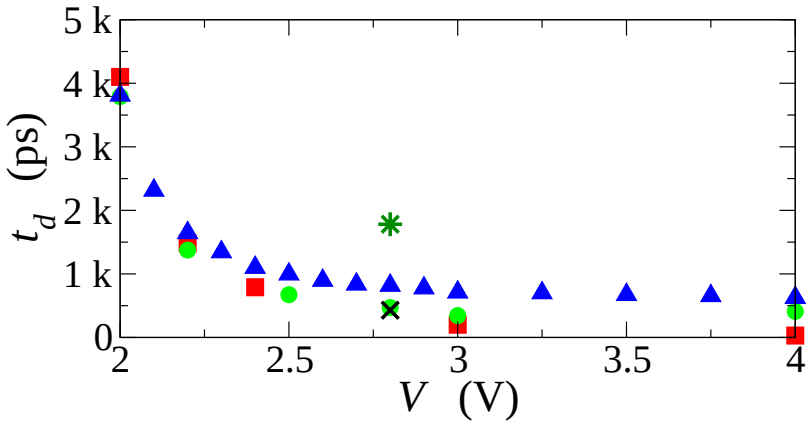

Figure 8. Simulated delay time t_d as a function of the amplitude of the applied signal V. The red squares and the green circles refer to the case where the input signal is applied directly to the PCM and consists of a voltage step or, respectively, of a trapezoidal voltage pulse like those of Fig. 5. The blue triangles refer to the case where the input signal (still a trapezoidal pulse) is applied through the circuit of Fig. 1, with $R_L = R_S = 1\ \Omega$ and $C = 300$ pF. The cross (star) shows the delay time for $V = 2.8$ V when the value of the capacitance is changed to 30 pF or 1000 pF, respectively.

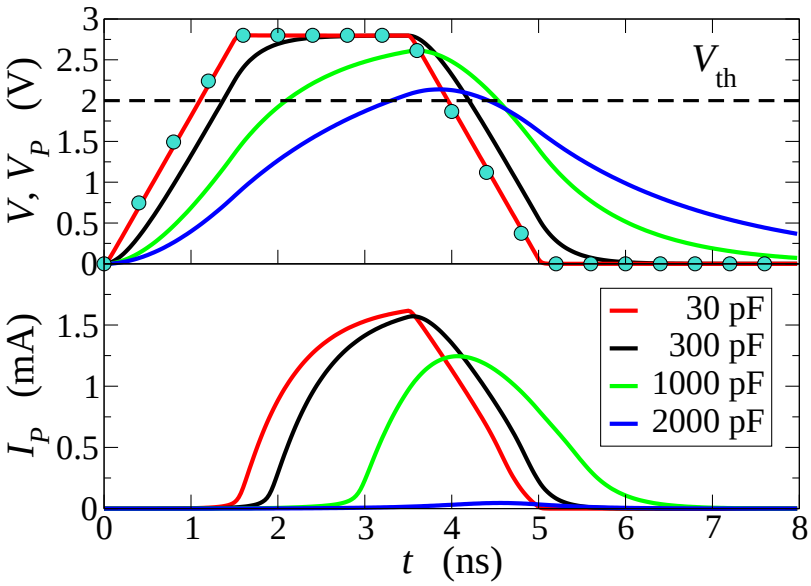

Figure 9. Simulated voltage drop V_P (above) and current I_P (below) of the PCM. The input signal V (above, circles) has a trapezoidal form with a plateau at 2.8 V, and is applied through the circuit of Fig. 1 with $R_L = R_S = 1\ \Omega$. Capacitance C is given different values as shown in the figure. The horizontal, dashed line marks the threshold voltage $V_{\rm th}$.

In agreement with what reported by (Saxena et al., 2021), ultrafast transient characteristics in the ns scale and below have been obtained in all considered cases. These results suggest that the delay time t_d, defined as the time elapsed between the instant at which the external bias exceeds the steady-state threshold value and the steep rise in the device current, varies in a wide range of values depending on the shape of the applied voltage. In particular, for plateau values significantly above threshold the carrier-heating process is very effective well before the maximum value of the voltage is reached; consequently, shorter delay times are observed (Fig. 5). Moreover, when the plateau value and the rise and fall times are fixed, the duration of the plateau influences the maximum value of the measured current, but does not affect the delay time (Figs. 6 and 7).

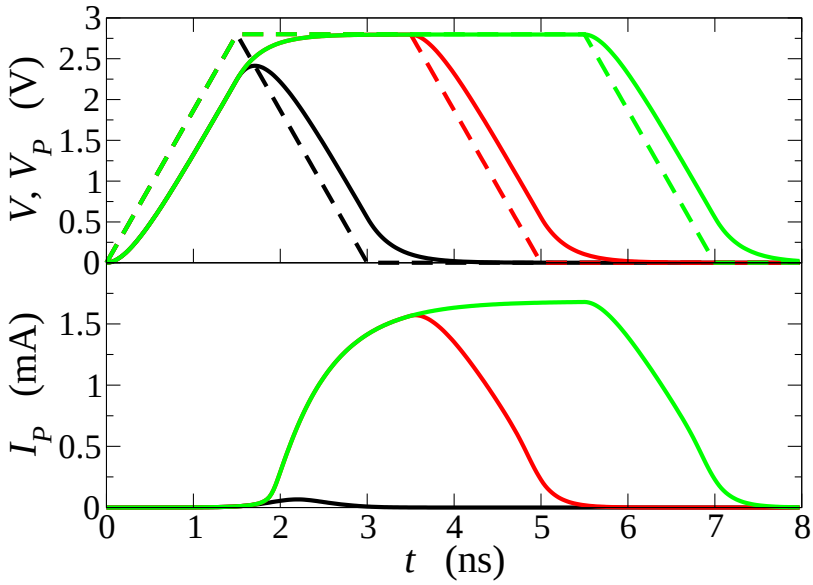

Figure 10. Same as in Fig. 9, with different durations of the plateau of V; the latter is set at 2.8 V, and capacitance C is set at 300 pF.

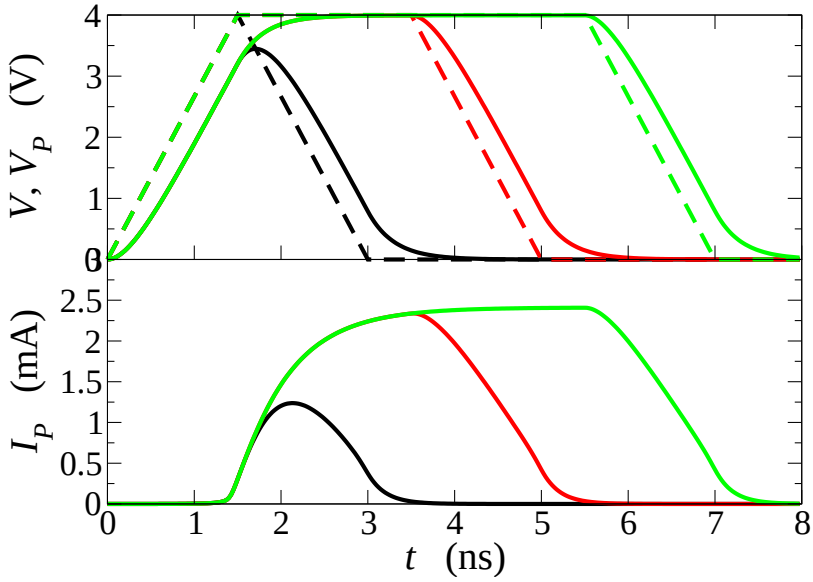

Figure 11. Same as in Fig. 10, with different durations of the plateau of V; here the latter is set at 4 V, and capacitance C is kept 300 pF.

All the above results are in agreement with those of (Saxena et al., 2021), and confirm the validity of a theoretical model for the OTS process based on purely electronic mechanisms. At least in absence of parasitic effects, and provided that the microscopic time constants of the chalcogenide in hand lie in the ns range and below, the speed of threshold switching in OTS devices can be pushed below the ns scale by a voltage pulse of suitable duration and value. Figure 8 summarises the results for the delay time t_d as a function of the applied voltage amplitude for the bias conditions considered so far. For rise and fall times of 1.5 ns, the delay times obtained for the step (red symbols) and trapezoidal profiles (green symbols) are almost overlapping near threshold, while at higher biases the response to the trapezoidal shape exhibits

still comparable, but longer delay times; this is probably due to a slower carrier heating process when the voltage ramps up the maximum value in about a ns.

3.3 The real world: finite rise and fall times, with parasitic effects

Parasitic effects connected to the measuring system and wirings can be minimized with a top level apparatus, but cannot be eliminated in full. To account for their contribution we have repeated the simulations of the delay time after embedding the PCM device into the circuit of Fig. 1, varying the equivalent capacitance C. The series resistances have been set at negligible values, since previous investigations pointed out a major modulating effect of the capacitance (Piccinini et al., 2016). The characteristic time of the circuit is thus proportional to $\tau_L = R_L\, C$, and acts as an additional delay time.

Figure 9 reports the voltage drop V_p across the PCM when the input signal has a trapezoidal form, with 1.5 rise and fall times, and a 2.8 V plateau with a 2 ns duration; the equivalent capacitance has been varied from 30 to 2000 pF. Due to the broadening of V_P (top panel), the higher the capacitance the shorter is the time interval during which $V_P > V_{\rm th}$. By way of example, $C = 2000$ pF corresponds to $\tau_L = 2$ ns, equal to the duration of the plateau; in this case the electronic switching is hindered (low panel), because the switching to the ON state occurs only if the applied signal is kept at its plateau value long enough, in such a way that the electronic processes described earlier can be activated and completed. Similar results are also shown in Figs. 10 and 11, where the duration of the plateau is increased from 0 to 4 ns, while the capacitance is kept fixed. Once again, the maximum voltage drop V_p is always larger than the threshold voltage but, if the signal drops soon after reaching the maximum value, the threshold switching does not occur (low panel of Fig. 10, black curve) or is incomplete (low panel of Fig. 11, black curve). These results are consistent with the findings of (Saxena et al., 2021).

For the sake of completeness we point out that the present transport model was developed for the amorphous OFF phase, and its parameters have been optimised for describing the subthreshold region. ON state currents are underestimated, and a quantitative comparison with the experimental currents also in the amorphous ON region preceeding the phase change would require a further model enhancement like, e.g., the inclusion of electron band states and the mobility increase that sets in when electrons coming from low-mobility states are excited to high-energy mobile states, and a consequent parameter recalibration. However, an even steeper rise of the current is expected not to alter appreciably the present findings.

In conclusion, we can split the measured delay time into two components: the former one is intrinsic to the switching phenomenon, and is associated to the time required to promote a significant number of carriers from localized to mobile states, thanks to carrier heating induced by the electric field (a similar change in the transport mechanism is also proposed in (Noé et al., 2017)); the latter component is instead depending on the measuring apparatus and wirings, and acts as a nearly rigid offset. This component can largely dominate if no particular care is taken in designing the circuitry. To support this statement, we see in Fig. 8 that increasing the capacitance by about three times nearly doubles the delay time.

A simplified analysis of the same issue has been carried out for comparison, with reference to the circuit of Fig. 1, and to the schematic model of the PCM characteristic of Fig. 2. The delay time t_d has been calculated from the relations of Sect. 2.4.2, using the same values of the lumped elements as those of Fig. 8. The S-shaped $I_P(V_P)$ characteristic of the PCM has been modeled with $R_1 = 1$ MΩ and $R_2 = 1$ kΩ,

a threshold voltage $V_{\rm th} = 2$ V, and a contact resistance $R_S = 1\ \Omega$. It is worth observing that, since the PCM is described with a static characteristic, here the delay is due to the combined effect of R_L and C (in other terms, there would be no delay if $R_L = 0$ and/or $C = 0$). The ramp slope $\alpha = 1.87 \times 10^9$ V/s ($\alpha = 2.67 \times 10^9$ V/s) corresponds to a rise time of 1.5 ns from $V = 0$ to $V = 2.8$ V ($V = 4$ V); it follows that $V = \alpha\, t$ becomes equal to the threshold voltage at $t' \simeq 1.07$ ns ($t' = 0.75$ ns).

The results are summarized in Tab. 2; one notes that, as expected, the same value of $\tau_L = R_L\, C$ provides the same value of t_d. Comparing with Fig. 8, one also notes that the delay times calculated as in Sect. 2.4.2 are lower (by a factor 2.5 at least) than those shown in Fig. 8. Remembering the discussion carried out in the first part of this section, this outcome is ascribed to the fact that, as the PCM characteristic of Fig. 2 is purely static, the expressions of Sect. 2.4.2 do not account for the additional delay due to the internal relaxation times of the PCM.

4 CONCLUSIONS

The delay time of the OTS onset, i.e., the delay between the instant at which the external voltage applied to the chalcogenide cell equals the static threshold voltage and the instant at which a steep rise of the current through the OTS device occurs, is a quantity that is strongly influenced by the time dependence of the applied voltage. This effect has been studied in this paper by means of theoretical approaches of different complexities, all based upon the assumption that OTS is mainly due to electronic effects.

A purely microscopic model based on a trap-limited transport scheme with appropriate microscopic parameters provides delay times below the ns limit, as recently measured in GST-225 cells (Saxena et al., 2021). The availability of new experimental results in the ns–ps time domain allows for a better tuning of the microscopic parameter τ_n, which greatly improves the theoretical quantitative results for the delay time with respect to our previous work (Jacoboni et al., 2017; Brunetti et al., 2020). Parasitic effects do not produce a noticeable increase of t_d, at least for suitably optimised, electrical-test systems like those used in advanced experiments. Based on the simulation tests performed with detailed microscopic models, an analytical, computationally efficient approach has been developed which captures the key features of the voltage-dependent transient characteristic of OTS devices, and is suitable for implementation into device-simulation tools.

The simulated transient currents are in substantial agreement with the experimental values obtained with similar external bias voltages, this confirming the existence of delay times in the sub-ns time scale on the basis of the physical process of carrier heating due to energy transfer from the external field. Analytical calculations confirm that, for realistic values of the parasitic parameters, the internal relaxation times of the PCM provide a non-negligible contribution to the delay time t_d.

CONFLICT OF INTEREST STATEMENT

The authors declare that the research was conducted in the absence of any commercial or financial relationships that could be construed as a potential conflict of interest.

AUTHOR CONTRIBUTIONS

All Authors have contributed equally to this work.

ACKNOWLEDGMENTS

The Authors gratefully acknowledge useful discussions with Prof. Anbarasu Manivannan and his team members.

TABLES

Table 1. Microscopic parameters of Eqs. (6), (7), (9), and (10). Apart from τ_n, the parameter values are taken from (Jacoboni et al., 2017).

Symbol	Definition	Value	Units
E_T	Energy level of traps	0	eV
E_B	Energy level of mobile states	0.35	eV
Δ	$E_B - E_T$		eV
g_T	DoS of trap states		eV^{-1}
g_B	DoS of mobile states		eV^{-1}
Γ	g_T/g_B	$2.5 \cdot 10^{-3}$	
γ	Coefficient of Poole effect	$3.36 \cdot 10^{-28}$	C m
ε	Relative permittivity of the material	15	
μ	Mobility of mobile electrons	$5.9 \cdot 10^{-4}$	$\mathrm{m}^2(\mathrm{V\,s})^{-1}$
n_0	Equilibrium electron concentration	$6.8 \cdot 10^{25}$	m^{-3}
τ_T	Temperature-relaxation time	$1.5 \cdot 10^{-13}$	s
τ_n	Recombination time	$0.6 \cdot 10^{-9}$	s
L	Device length	$53 \cdot 10^{-9}$	m
T_0	Room temperature	298	K

Table 2. Delay time t_d as a function of the lumped elements of Fig. 1. Symbol α indicates the slope of the ramp (see text).

R_L (Ω)	C (pF)	α (10^9 V/s)	t_d (ps)
1	30	1.87	30
1	300	1.87	297
1	1000	1.87	854
10	30	1.87	297
1	30	2.67	30
1	300	2.67	291
1	1000	2.67	784
10	30	2.67	291

REFERENCES

Servalli G. A 45nm generation Phase Change Memory technology. *IEEE International Electron Devices Meeting (IEDM), Technical Digest* (2009), 1–4.

[Dataset] Optane (2017a). http://techinsights.com/about-techinsights/overview/blog /intel-3D-xpoint-memory-die-removed-from-intel-optane-pcm/.

[Dataset] Optane (2017b). http://techinsights.com/about-techinsights/overview/blog /memory-selector-elements-for-intel-optane-xpoint-memory/.

[Dataset] Choe J. Memory/Selector Elements for Intel Optane^{TM} XPoint Memory (2017). http://techinsights.com/.

Arnaud F, Zuliani P, Reynard J, Gandolfo A, Disegni F, Mattavelli P, et al. Truly Innovative 28nm FDSOI Technology for Automotive Micro-Controller Applications embedding 16MB Phase Change Memory. *IEEE International Electron Devices Meeting (IEDM), Technical Digest* (2018), 18.4.1–18.4.4.

Markram H, Gerstner W, Sjöström PJ. A History of Spike-Timing-Dependent Plasticity. *Frontiers in Synaptic Neuroscience* **3** (2011) 4.

Le Gallo M, Sebastian A, Mathis R, Manica M, Giefers H, Tuma T, et al. Mixed-precision in-memory computing. *Nature Electronics* **1** (2018) 246–253.

Sebastian A, Le Gallo M, Khaddam-Aljameh R, Eleftheriou E. Memory devices and applications for in-memory computing. *Nature Nanotechnology* **15** (2020) 529–544.

[Dataset] Sarwat SG, Kersting B, Moraitis T, Jonnalagadda VP, Sebastian A. Phase Change Memtransistive Synapse (2021).

Lai S. Current status of the phase change memory and its future. *IEEE International Electron Devices Meeting (IEDM), Technical Digest* (2003), 10.1.1–10.1.4.

Raoux S, Wuttig M. *Phase Change Material —Science and Applications* (Springer) (2009).

Kolobov AV, Tominaga J. *Chalcogenides — Metastability and Phase Change Phenomena*. Materials Science (Springer) (2012).

Redaelli A, editor. *Phase Change Memory* (Springer) (2019).

Anbarasu M, Wimmer M, Bruns G, Salinga M, Wuttig M. Nanosecond threshold switching of $GeTe_6$ cells and their potential as selector devices. *Appl. Phys. Lett.* **100** (2012) 143505.

Wimmer M, Salinga M. The gradual nature of threshold switching. *New Journal of Physics* **16** (2014) 113044.

Shukla KD, Saxena N, Durai S, Manivannan A. Redefining the Speed Limit of Phase Change Memory Revealed by Time-resolved Steep Threshold-Switching Dynamics of Ag-In-Sb-Te Devices. *Sci. Rep.* **6** (2016) 37868.

Saxena N, Raghunathan R, Manivannan A. A scheme for enabling the ultimate speed of threshold switching in phase change memory devices. *Sci. Rep.* **11** (2021) 6111.

Shukla KD, Saxena N, Manivannan A. An ultrafast programmable electrical tester for enabling time-resolved, subnanosecond switching dynamics and programming of nanoscale memory devices. *Rev. Sci. Instrum.* **88** (2017) 123906.

Ielmini D. Threshold switching mechanism by high-field energy gain in the hopping transport of chalcogenide glasses. *Phys. Rev. B* **78** (2008) 035308.

Cappelli A, Piccinini E, Xiong F, Behnam H, Brunetti R, Rudan M, et al. Conductive preferential paths of hot carriers in amorphous phase-change materials. *Appl. Phys. Lett.* **103** (2013) 083503.

Buscemi F, Piccinini E, Cappelli A, Brunetti R, Rudan M, Jacoboni C. Electrical bistability in amorphous semiconductors: A basic analytical theory. *Appl. Phys. Lett.* **104** (2014a) 022101.

437 Brunetti R, Jacoboni C, Piccinini E, Rudan M. Band transport and localised states in modelling the electric
438 switching of chalcogenide materials. *J. Comp. Elect.* **19** (2020) 128.
439 Bogoslovskij NA, Tsendin KD. Electronic–thermal switching and memory in chalcogenide glassy
440 semiconductors. *J. of Non-Crystalline Solids* **357** (2011) 992–995.
441 Le Gallo M, Athmanathan A, Krebs D, Sebastian A. Evidence for thermally assisted threshold switching
442 behavior in nanoscale phase-change memory cells. *J. Appl. Phys.* **119** (2016) 025704.
443 Piccinini E, Brunetti R, Bordone P, Rudan M, Jacoboni C. Transient and oscillating response of ovonic
444 devices for high-speed electronics. *J. Phys. D: Appl. Phys.* **49** (2016) 495101.
445 Jacoboni C, Piccinini E, Brunetti R, Rudan M. Time- and space-dependent electric response of ovonic
446 devices. *J. Phys. D: Appl. Phys.* **50** (2017) 255103.
447 Poole HH. VIII. On the dielectric constant and electrical conductivity of mica in intense fields. *The*
448 *London, Edinburgh, and Dublin Philosophical Magazine and Journal of Science* **32** (1916) 112–129.
449 Ser. 6.
450 Ielmini D, Zhang Y. Analytical model for subthreshold conduction and threshold switching in
451 chalcogenide-based memory devices. *J. Appl. Phys.* **102** (2007) 054517.
452 Buscemi F, Piccinini E, Cappelli A, Brunetti R, Rudan M, Jacoboni C. Electrical bistability in amorphous
453 semiconductors: A basic analytical theory. *Appl. Phys. Lett.* **104** (2014b) 022101.
454 Press WH, Flannery BR, Teukolsky SA, Wetterling WT. *Numerical Recipes — The Art of Scientific*
455 *Computing* (New York: Cambridge University Press) (1988).
456 Noé P, Vallée C, Hippert F, Fillot F, Raty JY. Phase-change materials for non-volatile memory devices:
457 from technological challenges to materials science issues. *Semicond. Sci. Technol.* **33** (2017) 013002.